Normal modes of spin excitations in magnetic nanoparticles

Marcos Grimsditch*
Materials Science Division, Argonne National Laboratory, Argonne, Illinois 60439, USA

Gary K. Leaf,† Hans G. Kaper,‡ and Dmitry A. Karpeev§
Mathematics and Computer Science Division, Argonne National Laboratory, Argonne, Illinois 60439, USA

Robert E. Camley¶
Department of Physics and Energy Science, University of Colorado, Colorado Springs, Colorado 80918, USA
(Received 27 May 2003; revised manuscript received 21 November 2003; published 28 May 2004)

This paper describes a technique to compute magnetic normal modes of nanosized particles. The technique is based on the Landau-Lifshitz formalism of micromagnetics and accounts fully for both the exchange and the dipolar field. It requires no more than the specification of the material parameters and the geometry of the sample; in particular, it does not require the specification of boundary conditions. It also allows the large-amplitude nonlinear regime to be probed. The technique is applied to a model of a polycrystalline iron particle, which is shown to possess a rich variety of normal modes. Some of these modes are reminiscent of standing waves, while others are more or less localized in parts of the sample. The variation of the mode frequencies with the applied field is analyzed and compared with existing approximations.

DOI: 10.1103/PhysRevB.69.174428 PACS number(s): 75.40.Mg, 75.40.Gb, 75.75.+a

I. INTRODUCTION

Recent advances in processing techniques have made it possible to fabricate small magnetic particles with accurate control over their shape and thickness.[1–6] Because the size of such particles can be comparable to the exchange length or the domain wall thickness, their magnetic behavior differs fundamentally from that of larger samples, where the existence of multiple magnetic domains plays a fundamental role. While the dynamics of magnetic spins in nanoparticles have been addressed experimentally by means of Brillouin scattering, ferromagnetic resonance (FMR), and other novel techniques, much less work has been done on the corresponding theoretical problem of determining magnetic normal modes. This problem is of more than theoretical importance; indeed, it has important implications for technology. For example, the reduction in size of a read head is ultimately limited by spin-wave induced noise.[7] If the normal modes were known, one could control them by suitable design choices, thus limiting the noise and enabling further size reductions.

Attempts to solve the magnetic normal-mode problem in a manner analogous to that used for mechanical normal modes of vibration of a finite particle have been mostly unsuccessful. The problem is difficult because one must account simultaneously for the exchange coupling, which acts at the atomic level, and dipolar fields that are typically long range and extend over the whole sample. Only in a very few special cases and under severely restricting conditions is it possible to treat the problem analytically. If both exchange and dipolar fields are included, the normal modes are known only for the homogeneous saturated infinite bulk ferromagnet;[8] if exchange is neglected, they are known for the homogeneous infinite magnetic slab[9,10] and, with certain additional approximations, for a few very simple shapes;[11,12] and only if dipolar fields are neglected entirely can they be obtained for more general cases.[13] Very recently, some progress has been made in evaluating magnetic modes in confined geometries when dipolar induced pinning effects are included.[14–17]

In the absence of analytical solutions, computations offer the only feasible alternative. The purpose of this paper is to show how, on the basis of the Landau-Lifshitz formalism of micromagnetics,[18] magnetic normal modes of nanosized particles can be identified in the presence of both exchange and dipolar fields. Support for this idea comes from earlier work on micromagnetic-based FMR computations,[19–21] where the FMR frequency of a small saturated flat disk was determined from a Fourier transform of the time-dependent total magnetization. The proposed computational procedure has three significant features. First, the particle is divided into cells whose dimensions are smaller than the exchange length, so the magnetization within a cell is approximately uniform. The spatial approximations are then based on finite differences. Second, the algorithm used to integrate the Landau-Lifshitz equation maintains a constant magnetization at all times. The algorithm is the same as the one used by the authors for spring-magnet calculations.[22] Third, the dipolar (far-field) contribution is derived from a scalar magnetic potential, and the latter is computed by means of a boundary integral formulation. Thus, the computational domain is the same as the physical domain occupied by the particle, and there is no need to artificially extend the domain or introduce artificial boundary conditions.

The plan of this paper is as follows. In Sec. II, we formulate the micromagnetics problem and describe the computational approach to identify magnetic normal modes. In Sec. III, we present the results of numerical simulations for a polycrystalline iron nanoparticle. We identify several normal modes and analyze the behavior of their frequency as a function of the strength of the applied field. In Sec. IV, we summarize our findings and discuss the type of problems that can be addressed with the current method.

II. MICROMAGNETIC MODEL

The Landau-Lifshitz (LL) equation of micromagnetics is a differential equation for the magnetization vector $\boldsymbol{M}$,

$$\frac{\partial \boldsymbol{M}}{\partial t} = -\frac{\gamma}{1+g^2}\left[(\boldsymbol{M}\times\boldsymbol{H}) + \frac{g}{M}\boldsymbol{M}\times(\boldsymbol{M}\times\boldsymbol{H})\right]. \tag{1}$$

Here, $\boldsymbol{H}$ is the effective magnetic field, which depends nonlinearly on $\boldsymbol{M}$, and M is the magnitude of $\boldsymbol{M}$. Equation (1) is the equation of a spinning top driven by the magnetic field (first term inside the brackets) and subject to damping (second term); γ is the gyromagnetic constant and g a (dimensionless) damping coefficient. The LL equation maintains a constant magnetization; $M = M_s$ at all times, where M_s is the saturation magnetization. On the other hand, the direction of $\boldsymbol{M}$, which is given by the magnetic spin vector $\boldsymbol{m} = \boldsymbol{M}/M$, varies with time t, as well as with space throughout the sample.

A. Time integration of the Landau-Lifshitz equation

The time integration of the LL equation requires special care, since it is essential that the magnitude of the magnetization be preserved at all times. The algorithm that accomplishes this has been described elsewhere,[22] but we include a brief description here for completeness.

We begin by observing that the spatial variation does not play a role in the time integration of the LL equation, so the following description applies anywhere in the domain. To emphasize this point, we focus on time as the independent variable and use a prime $'$ to denote (partial) differentiation with respect to time.

Next, we separate the magnitude of the effective magnetic field from its direction, writing $\boldsymbol{H} = H\boldsymbol{h}$, where $H = |\boldsymbol{H}|$. Thus $\boldsymbol{h}$, like $\boldsymbol{m}$, is a vector of unit length. Then the LL equation assumes the form

$$\boldsymbol{m}' = -cH[(\boldsymbol{m}\times\boldsymbol{h}) + g\boldsymbol{m}\times(\boldsymbol{m}\times\boldsymbol{h})], \tag{2}$$

where $c = \gamma/(1+g^2)$ is a constant.

We can rewrite the LL equation as two separate equations if we introduce, for any three-component vector $\boldsymbol{u}$ the projections P and Q,

$$P\boldsymbol{u} = (\boldsymbol{u}\cdot\boldsymbol{h})\boldsymbol{h}, \quad Q\boldsymbol{u} = \boldsymbol{u} - P\boldsymbol{u} = \boldsymbol{h}\times(\boldsymbol{u}\times\boldsymbol{h}). \tag{3}$$

Applying P and Q to Eq. (2), we obtain

$$P\boldsymbol{m}' = -cHP[(\boldsymbol{m}\times\boldsymbol{h}) + g\boldsymbol{m}\times(\boldsymbol{m}\times\boldsymbol{h})], \tag{4}$$

$$Q\boldsymbol{m}' = -cHQ[(\boldsymbol{m}\times\boldsymbol{h}) + g\boldsymbol{m}\times(\boldsymbol{m}\times\boldsymbol{h}). \tag{5}$$

Notice the identities

$$P(\boldsymbol{m}\times\boldsymbol{h}) = 0,$$

$$P[\boldsymbol{m}\times(\boldsymbol{m}\times\boldsymbol{h})] = (\boldsymbol{m}\cdot Q\boldsymbol{m})\boldsymbol{h} = -[1-(P\boldsymbol{m}\cdot P\boldsymbol{m})^2]\boldsymbol{h},$$

$$Q(\boldsymbol{m}\times\boldsymbol{h}) = -JQ\boldsymbol{m},$$

$$Q[\boldsymbol{m}\times(\boldsymbol{m}\times\boldsymbol{h})] = (\boldsymbol{m}\cdot\boldsymbol{h})Q\boldsymbol{m},$$

where J is the square root of the negative identity in $\mathbf{R}^2$,

$$I = \begin{pmatrix} 1 & 0 \\ 0 & 1 \end{pmatrix}, \quad J = \begin{pmatrix} 0 & -1 \\ 1 & 0 \end{pmatrix}, \quad J^2 = -I.$$

Hence, we can recast Eqs. (4) and (5) in the form

$$P\boldsymbol{m}' = cgH[1-(P\boldsymbol{m}\cdot P\boldsymbol{m})^2]\boldsymbol{h}, \tag{6}$$

$$Q\boldsymbol{m}' = cH[J - g(\boldsymbol{m}\cdot\boldsymbol{h})I]Q\boldsymbol{m}. \tag{7}$$

Now, suppose that $\boldsymbol{H}$ does not change on a time interval $[t, t+\Delta t]$,

$$\boldsymbol{H}(s) = \boldsymbol{H}(t), \quad t \leqslant s \leqslant t+\Delta t. \tag{8}$$

Then $P\boldsymbol{m}' = (P\boldsymbol{m})'$ and $Q\boldsymbol{m}' = (Q\boldsymbol{m})'$ on $[t, t+\Delta t]$, so Eqs. (6) and (7) reduce to a coupled system of differential equations for the scalar $u = (P\boldsymbol{m}\cdot\boldsymbol{h})$ and the vector $\boldsymbol{v} = Q\boldsymbol{m}$,

$$u' = cgH(1-u^2) \quad \text{on} \quad [t, t+\Delta t]. \tag{9}$$

$$\boldsymbol{v}' = cH(J - guI)\boldsymbol{v} \quad \text{on} \quad [t, t+\Delta t]. \tag{10}$$

The equation for u is independent of $\boldsymbol{v}$; it can be integrated exactly,

$$u(s) = \frac{u(t)\cosh(cgH(t)(s-t)) + \sinh(cgH(t)(s-t))}{\cosh(cgH(t)(s-t)) + u(t)\sinh(cgH(t)(s-t))} \tag{11}$$

for $t \leqslant s \leqslant t+\Delta t$.

Next, we turn to Eq. (10). We replace the constant cgH by $u'/(1-u^2)$ [from Eq. (9)] and use the identity $-uu'/(1-u^2) = [\ln(1-u^2)^{1/2}]'$ to convert the equation into a differential equation for the vector $\boldsymbol{w} = (1-u^2)^{-1/2}\boldsymbol{v}$,

$$\boldsymbol{w}' = cHJ\boldsymbol{w} \quad \text{on} \quad [t, t+\Delta t]. \tag{12}$$

This equation can be integrated,

$$\begin{aligned} \boldsymbol{w}(s) &= e^{cH(t)(s-t)J}\boldsymbol{w}(t) \\ &= [\cos(cH(t)(s-t))I + \sin(cH(t)(s-t))J]\boldsymbol{w}(t) \end{aligned} \tag{13}$$

for $t \leqslant s \leqslant t+\Delta t$. From the expression (11) we obtain

$$(1-u(s)^2)^{1/2} = \frac{[1-u(t)^2]^{1/2}}{\cosh(cgH(t)(s-t)) + u(t)\sinh(cgH(t)(s-t))},$$

so

$$\boldsymbol{v}(s) = \frac{\cos(cH(t)(s-t))I + \sin(cH(t)(s-t))J}{\cosh(cgH(t)(s-t)) + u(t)\sinh(cgH(t)(s-t))}\boldsymbol{v}(t) \tag{14}$$

for $t \leqslant s \leqslant t+\Delta t$.

These results motivate the choice of the integration scheme for Eq. (2),

$$\boldsymbol{m}_{n+1} = \alpha_n\boldsymbol{h}_n + \beta_n\boldsymbol{h}_n(\boldsymbol{m}_n\times\boldsymbol{h}_n), \tag{15}$$

where $\boldsymbol{m}_{n+1} = \boldsymbol{m}(t_{n+1})$, $\boldsymbol{m}_n = \boldsymbol{m}(t_n)$, $\boldsymbol{h}_n = \boldsymbol{h}(t_n)$, and

$$\alpha_n = \frac{(\boldsymbol{m}_n \cdot \boldsymbol{h}_n)\cosh(cgH_n\Delta t) + \sinh(cgH_n\Delta t)}{\cosh(cgH_n\Delta t) + (\boldsymbol{m}_n \cdot \boldsymbol{h}_n)\sinh(cgH_n\Delta t)},$$

$$\beta_n = \frac{\cos(cH_n\Delta t)I + \sin(cH_n\Delta t)J}{\cosh(cgH_n\Delta t) + (\boldsymbol{m}_n \cdot \boldsymbol{h}_n)\sinh(cgH_n\Delta t)},$$

with $H_n = H(t_n)$ and $\Delta t = t_{n+1} - t_n$.

The algorithm (15) is unconditionally stable for all values of Δt. Of course, the quality of the approximation suffers as Δt increases. However, the algorithm explicitly displays the relationship between the size of Δt and the local error in the time integration. The rate of precession of $\boldsymbol{m}$ around the polar axis is governed by H, the magnitude of the local effective field: in one time step, $\boldsymbol{m}$ precesses through an angle $H\Delta t$. Therefore, by properly choosing Δt, we can resolve the fastest precessional motion in a given number of time steps per period. Since H varies over the course of a simulation, we have a natural and direct means to adjust the size of Δt to the current dynamical state, while maintaining the resolution of the precessional motion.

Other algorithms for the numerical integration of the LL equation have been proposed by Chen, Fredkin, and Koehler,[23] Nigam[24] and E and Wang.[25]

B. The effective magnetic field

The effective magnetic field $\boldsymbol{H}$ is derived from the free energy, E. If $\boldsymbol{H}_a$ is the externally applied magnetic field, then

$$\boldsymbol{H} = -\frac{\delta E}{\delta \boldsymbol{M}}. \tag{16}$$

If anisotropy contributions and magnetostrictive terms are ignored (an assumption that is certainly justified in the case of polycrystalline materials), the free energy is the sum of the exchange energy, the (dipolar) far-field energy, and the energy contribution from the applied field,

$$E = E_{\mathrm{ex}} + E_{\mathrm{ff}} + E_{\mathrm{af}}. \tag{17}$$

The individual terms are given by the integrals

$$E_{\mathrm{ex}} = \int A|\nabla \boldsymbol{M}|^2, \tag{18a}$$

$$E_{\mathrm{ff}} = -\frac{1}{2}\int \boldsymbol{M} \cdot \boldsymbol{H}_{\mathrm{ff}}, \tag{18b}$$

$$E_{\mathrm{af}} = -\int \boldsymbol{M} \cdot \boldsymbol{H}_a, \tag{18c}$$

where A is the exchange coupling constant.

The exchange energy contributes a term proportional to $\Delta \boldsymbol{M}$ to the effective-field subject to the natural boundary condition (vanishing interior limit of the normal derivative). The Laplacian is approximated numerically by means of the standard 7-point stencil.

The far field is obtained from a scalar magnetic potential, $\boldsymbol{H}_{\mathrm{ff}} = -\nabla\Phi$, which, given the magnetization $\boldsymbol{M}$, is calculated as follows.[26] First, Φ is written as a sum, $\Phi = \Phi_1 + \Phi_2$, where Φ_1 is the solution of the Neumann problem

$$\Delta\Phi_1 = 4\pi(\nabla \cdot \boldsymbol{M}) \text{ in } \Omega, \quad \boldsymbol{n} \cdot \nabla\Phi_1 = 4\pi(\boldsymbol{n} \cdot \boldsymbol{M}) \text{on } \partial\Omega. \tag{19}$$

Here, Ω is the domain, $\partial\Omega$ is the boundary of Ω, and $\boldsymbol{n}$ is the outward normal on the boundary. The boundary values of Φ_1 thus obtained generate the boundary values of Φ_2,

$$\Phi_2(\boldsymbol{x}) = \int_{\partial\Omega} \Phi_1(\boldsymbol{y}) \cos\left[\boldsymbol{n} \cdot \frac{\boldsymbol{x}-\boldsymbol{y}}{|\boldsymbol{x}-\boldsymbol{y}|}\right], \quad \boldsymbol{x},\boldsymbol{y} \in \partial\Omega, \tag{20}$$

and Φ_2 is found by solving the Dirichlet problem $\Delta\Phi_2 = 0$ in Ω subject to the computed boundary values.

C. Computational approach

We assume that the domain Ω (the physical domain occupied by the particle) is three dimensional and rectangular and that the particle is placed in a Cartesian (x,y,z) coordinate system, with $\boldsymbol{M} = (M_x, M_y, M_z)$. The applied magnetic field is uniform, constant in time, and directed along the positive x axis, $\boldsymbol{H}_a = (H_a, 0, 0)$.

The particle is divided into cubic cells, and the magnetization is assumed to be uniform in each cell. A cell is indexed by a triplet (i,j,k), and each cell carries a magnetization vector $\boldsymbol{M}_{i,j,k}$. The magnitude of $\boldsymbol{M}_{i,j,k}$ is constant and equal to the saturation magnetization M_s; its direction is given by the spin vector $\boldsymbol{m}_{i,j,k}$, which is a vector of unit length.

Given the dimensions of the particle and the strength of the applied magnetic field, the only physical parameters that need to be specified for the simulations are the exchange coupling constant A, the saturation magnetization M_s, the gyromagnetic constant γ, and the damping coefficient g.

The approach used to find normal modes is conceptually similar to the one used previously in FMR calculations.[19,20] For a given applied field, the particle is first allowed to reach its equilibrium state. This is accomplished by integrating the LL equation (1) to equilibrium with the damping coefficient $g = 0.5$. The spin configuration is then perturbed from equilibrium and, with the damping coefficient $g = 0$, allowed to evolve in time. The motion of each spin vector is monitored at regular intervals for a certain length of time, and the time series of each component in each cell is Fourier analyzed. (In Ref. 19, the Fourier transform was applied only to the spatially averaged magnetization vector.) The normal modes are then identified by correlating the Fourier transforms throughout the sample.

Typically, a spin vector describes an elliptically shaped closed orbit in a plane. The orbit plane and the orbit center reflect the static equilibrium configuration of the magnetization; they are the same for all modes and need not be considered further. The dynamics of a particular mode at a given frequency are specified completely by four parameters for each cell, namely, the area of the spin orbit, its aspect ratio (ratio of major to minor axis), its tilt (angle between major axis and sample axes), and the relative phase of the spin vectors. The numerical simulations indicate that well defined correlations between cells emerge only at frequencies where

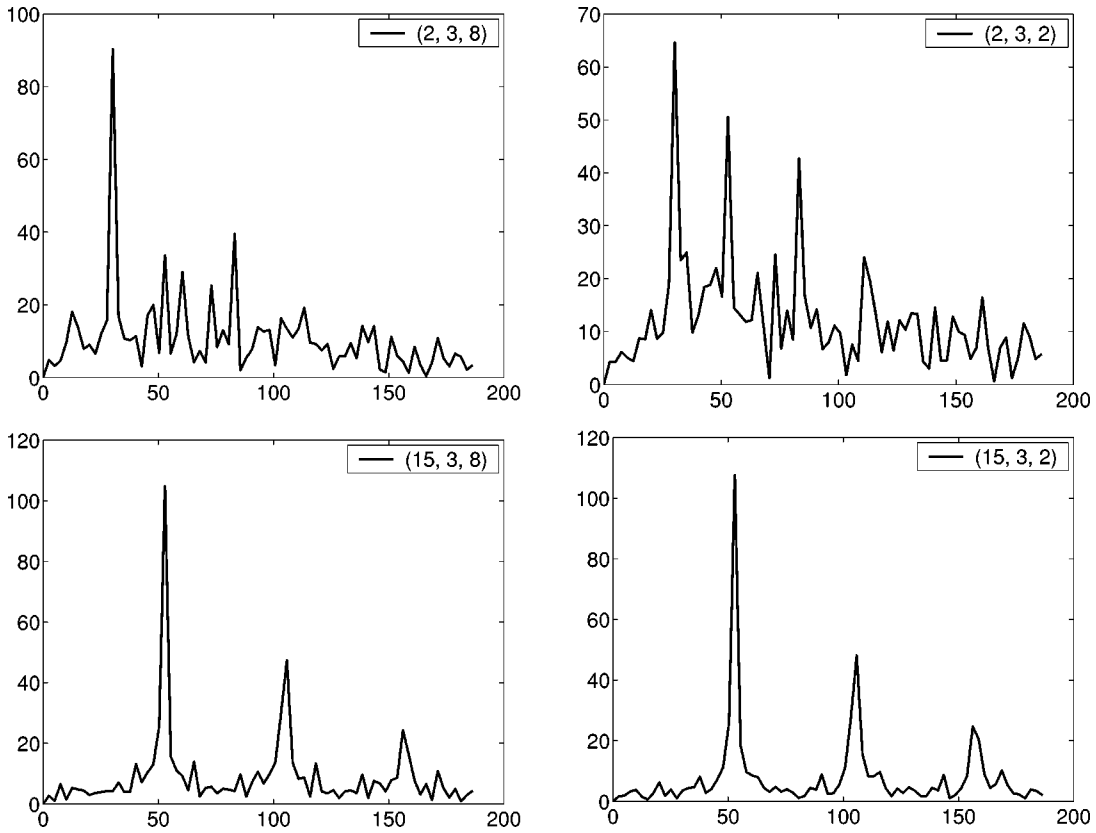

FIG. 1. Fourier transform of M_z vs frequency (GHz) in four cells in the midplane.

at least some cells show clear peaks in the Fourier transform; when there are no peaks in any cell, no correlations are observed.

A complete description of a magnetic normal mode in terms of the four parameters for each cell is clearly impractical. How to devise a description in terms of a few parameters is, however, not obvious. It is helpful to compare the current problem with the analogous problem for normal modes of a vibrating membrane. The latter is described by an expression of the form $AF(\boldsymbol{x})e^{i\omega t}$, where A is a scalar amplitude and F a normalized function of position (for example, a Bessel function in the case of a circular membrane). A snapshot of a membrane oscillating in an eigenmode provides a complete representation of $F(\boldsymbol{x})$ and, thus, a characterization of the normal mode. In the present case, the problem is more complicated. The time and space variables are not separable, the amplitude is a vector, and the function F is different for each component. In principle, one can adopt the same approach as for the vibrating membrane and use a snapshot of one of the components of the magnetization. This approach gives an intuitively clear picture of a mode, but the result must be interpreted with care. Because of the phase differences between cells, snapshots at different times are not necessarily comparable; moreover, the amplitudes do not scale, and slight differences in the profiles will be present; and finally, changes in the aspect ratio will produce variations between snapshots of different components of the magnetization. For these reasons it is prudent to give additional consideration to the area of the spin orbit in each cell to corroborate the results obtained from a snapshot of one of the components of the magnetization. The orbit area is proportional to the amplitude and therefore independent of time, a fact that is convenient. A shortcoming of this representation is, of course, that it does not contain information about the phase of the spin.

III. RESULTS FOR A POLYCRYSTALLINE IRON PARTICLE

In this section, we present the results of numerical simulations for a model of a polycrystalline iron particle. The sample is rectangular, measuring $116\times20\times60$ nm^3, and the material parameters are

$$A=2.5\times10^{-6}\ \text{erg/cm},$$

$$M_s=1{,}700\ \ \text{emu/cm}^3(=\text{oersted}),$$

$$\gamma=2.93\ \ \text{GHz/kOe}.$$

The particle is placed in a uniform magnetic field, which is constant in time and directed along the positive x axis, $\boldsymbol{H}_a=(H_a,0,0)$. The particle is arranged so the field is lined up with the long (116) side, the short (20) side is aligned with the y axis, and z is the coordinate in the spanwise (60) direction. The particle is divided into cubic cells measuring 4 nm on a side. Each cell is indexed by a triplet (i,j,k), with $i=1,\ldots,29$; $j=1,\ldots,5$; and $k=1,\ldots,15$. The total number of cells is $29\times5\times15=2{,}175$.

Once equilibrium is achieved, a perturbation is applied to excite the normal modes. A given perturbation will excite

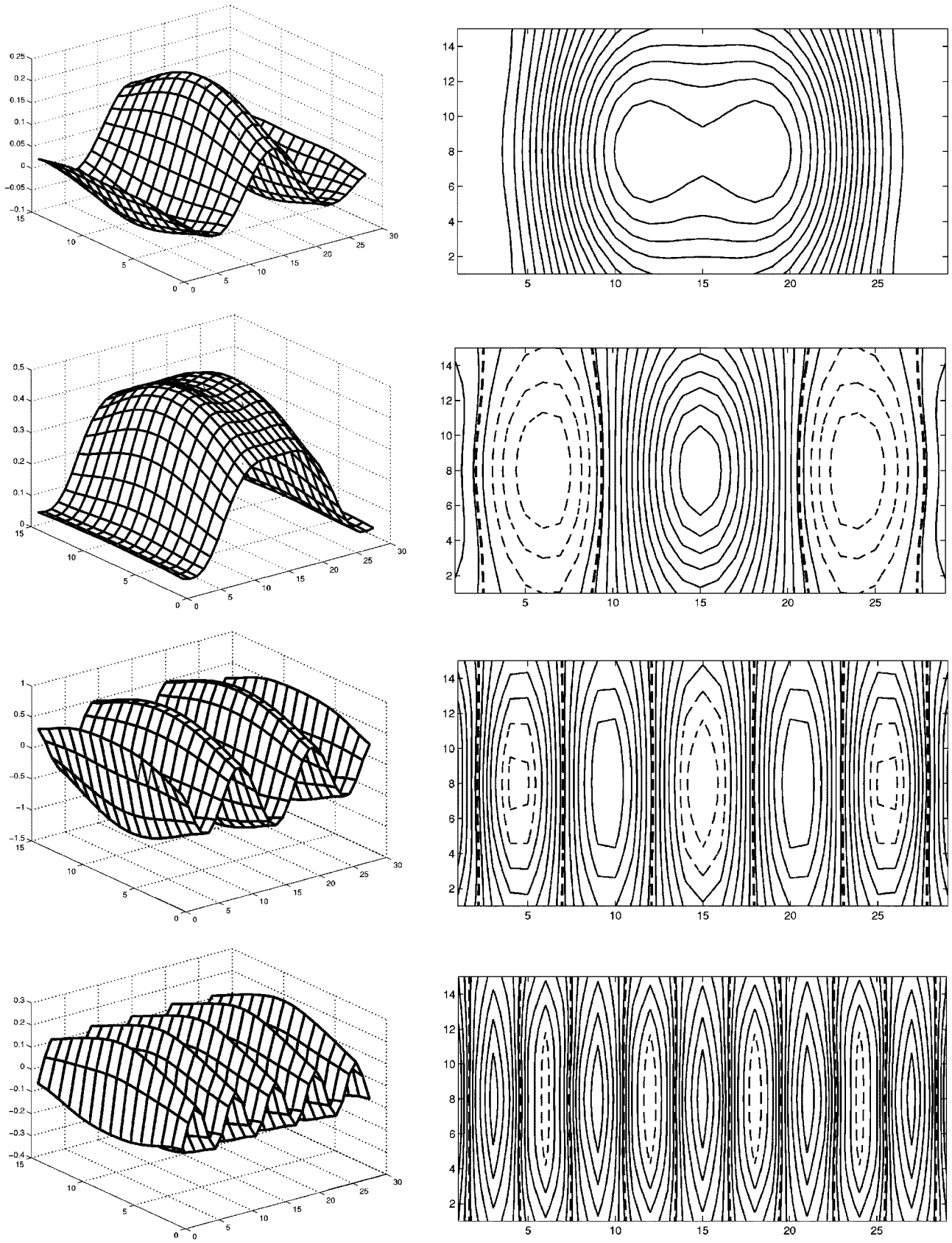

FIG. 2. Four symmetric one-dimensional plane-wave-like normal modes. From top to bottom: 4-node mode (49 GHz), 0-node mode (52 GHz), 6-node mode (57 GHz), and 10-node mode (89 GHz).

only those modes whose spatial Fourier transform is contained in that of the perturbation. This feature has both advantages and disadvantages. By judiciously choosing the perturbation, one can reduce the number of excited modes and thus avoid excessive mode overlap. On the other hand, numerous simulations must be performed to guarantee that all the modes are actually observed. We have chosen to work with two perturbations, one symmetric, the other antisymmetric along the long axis (the direction of the applied field). In the symmetric perturbation, the spins in the central portion of the particle—that is, in all cells with $i=7,\ldots,23$—are rotated from their equilibrium position by 1 deg in the (x,z) plane. In the antisymmetric perturbation, the spins in the cells with $i=7,\ldots,14$ are rotated by 1 deg in the positive direction and those with $i=16,\ldots,23$ by 1 deg in the negative direction. The numerical simulations indicate that, as long as the perturbations do not exceed ± 5 deg, the position of a peak in the frequency spectrum is not affected. We also ascertained that the Fourier amplitude of a peak scales with the amplitude of the initial perturbation, so we are clearly probing the response in the linear regime. The Fourier transform can be performed on any of the components of the spin vector; again, the choice of the particular component affects the relative amplitudes of the peaks but not their positions in the frequency spectrum.

All the results reported below were obtained by integrating the LL equations over a period of 11.88×10^{-10} sec. The resulting frequency resolution in the Fourier transform is 0.63 GHz.

A. Fixed applied field, $H_a=10$ kOe

We first probe the normal-mode structure of the nanoparticle at a fixed value of the applied field, $H_a=10$ kOe. The dependence on the strength of the applied field will be taken up in Sec. III B.

Figure 1 shows the Fourier transform of M_z in four representative cells in the midplane $(j=3)$ after a symmetric perturbation. The graphs on the left are for cells near the end of the particle $(i=2)$, the graphs on the right are for cells midway along the long axis $(i=15)$. A peak in the Fourier transform indicates that the initial perturbation has excited a mode in the particular cell at that frequency and indicates the existence of a normal mode at that frequency. (The converse is not necessarily true. The absence of a peak may simply indicate that the normal mode at that frequency has a small amplitude in that cell. Therefore, while it is possible to be guided by peaks in individual Fourier transforms, the only fail-safe technique is to reconstruct the modes at every frequency of the Fourier transform and then ignore those that are weak and show no clear structure.) The differences between the Fourier transforms in cells near the edges and in the center of the sample already provide evidence that edge effects play an important role in determining the normal-mode structure.

The graphs in Fig. 2 show four one-dimensional plane-wave-like normal modes, both in three-dimensional perspective (left column) and as two-dimensional contour plots (right column). They were obtained by plotting the Fourier transform of M_z in the midplane $(j=3)$ against i (horizontal axis) and k (vertical axis). From top to bottom, we observe a 4-node mode at 49 GHz, a 0-node mode at 52 GHz, a 6-node mode at 57 GHz, and a 10-node mode at 89 GHz. (Modes with an odd number of nodes are not excited by the symmetric initial perturbation.) Excluding the 0-node mode, we note that the mode frequency increases with the number of nodes, as expected from the exchange interaction. The 0-node mode is reminiscent of the uniform (FMR) mode in a bulk sample and is referred to as the ''bulk'' mode. Its frequency is close to the FMR frequency, and its amplitude is fairly uniform throughout the interior of the sample. This mode would become the uniform mode if the sample were made infinitely large. Contrary to the FMR mode, however, its phase differs by almost 30 deg between the ends and the center of the sample. (In an infinite film, the phase of the FMR mode is constant throughout the sample.) The other modes in Fig. 2 show a clearly identifiable standing-wave-like structure in the direction of the applied field. The existence of standing waves in confined geometries is well known.[14–16,27,28] Their theoretical explanation requires the introduction of *ad hoc* boundary conditions at the free surfaces, which has led to the concept of ''pinning''[27,28] and the definition of the Rado-Weertman boundary conditions.[29] The physical origin of pinning is usually ascribed to surface anisotropy, although it has been correlated more recently with the local demagnetizing field in the vicinity of edges.[15,16] The present approach does not require any such *ad hoc* boundary conditions. Figure 2 shows that the bulk mode is ''pinned'' at the ends, the 4-node mode is almost pinned, but the other two modes are essentially unpinned. We return to this point in Sec. III C, where we discuss the dependence of the mode frequencies on the wavelength.

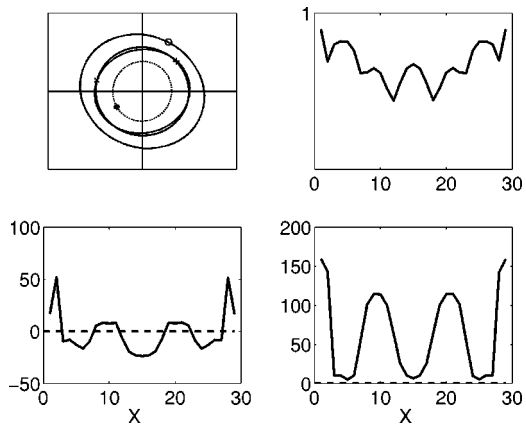

FIG. 3. Details of the spin motion for the 6-node mode. Top left: four spin orbits in the (x,z) plane in different cells along the long axis. The three other graphs show the variation of the aspect ratio (top right), tilt of the major axis (in degrees, bottom left), and relative phase (in degrees, bottom right) along the major (x) axis.

The graphs in Fig. 2 were obtained by taking snapshots of one component (M_z) of the magnetization vector. As mentioned in the preceding section, these snapshots provide only a partial description. Figure 3 provides a more complete description of the 6-node mode shown in Fig. 2. The top left diagram in Fig. 3 shows the spin orbits in four cells (i

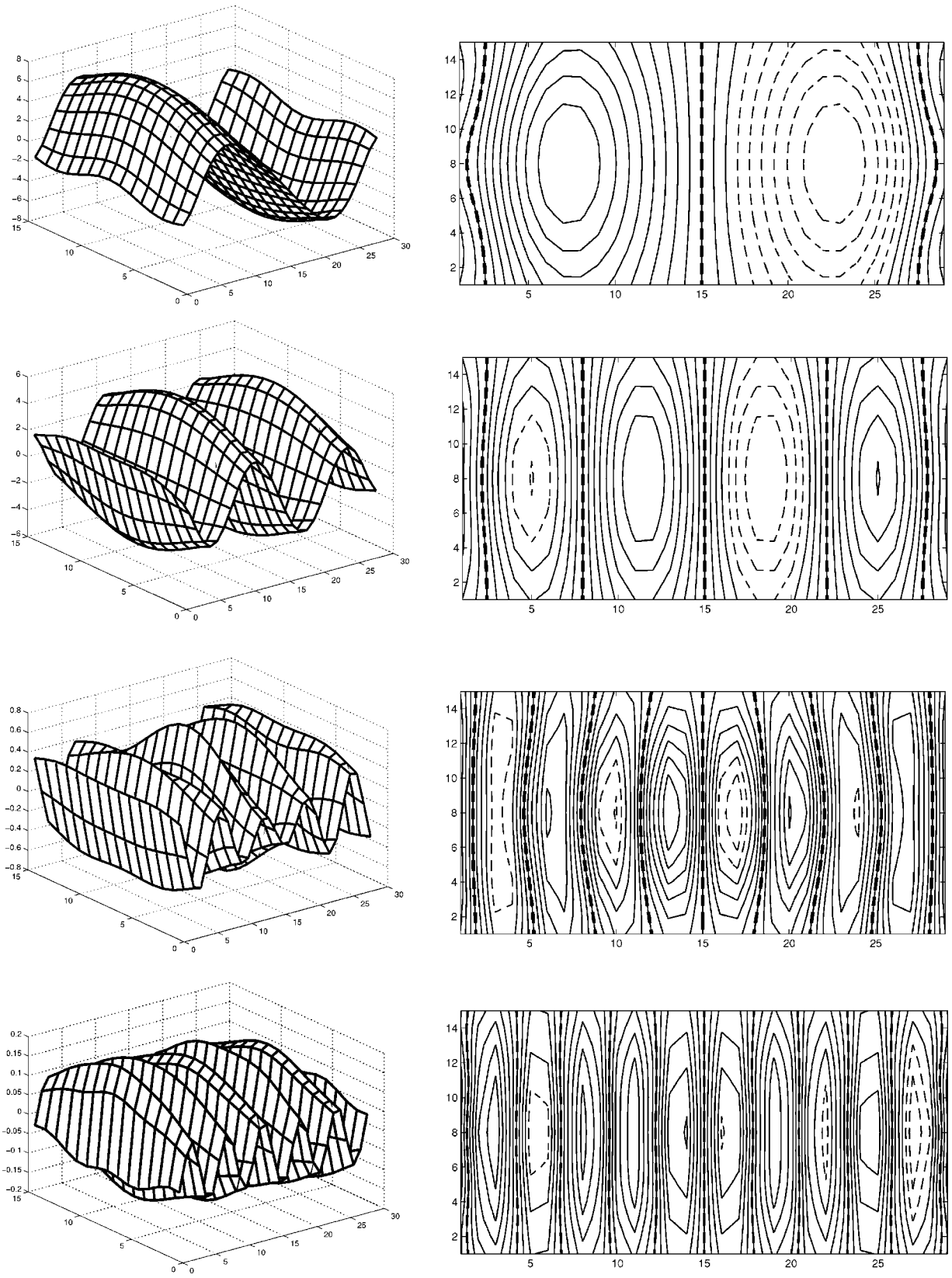

FIG. 4. Four antisymmetric standing-wave-like modes. From top to bottom: 3-node mode (49 GHz), 5-node mode (52 GHz), 9-mode node (80 GHz), and 11-node mode (99 GHz).

$=1,4,9,14$) along the major axis of the sample. The mark on each orbit indicates the position of the spin vector at a given instant of time, from which the relative phases can be inferred. The graph at the bottom right shows the variation of the phase along the long (x) axis. The remaining two graphs in Fig. 3 show the variation of the aspect ratio and the tilt of the major axis of the orbit along the x axis. In a simple ''standing-wave'' picture, the aspect ratio would be a constant, the tilt would be zero, and the phase would jump discontinuously by 180 deg at every node. Clearly, the mode in our particle does not have any of these simplifying attributes.

The antisymmetric perturbation excites a different set of modes. Figure 4 shows four one-dimensional plane-wave-like modes, again arranged from top to bottom in order of increasing frequency. The lowest frequency is associated with a 3-node mode (49 GHz), next is a 5-node mode (52 GHz), followed by a 9-node mode (80 GHz), and an 11-node mode (99 GHz). Clearly, the frequency increases with the number of nodes. As expected, only modes with an odd number of nodes are observed, and every antisymmetric mode has a node at the center. A more interesting observation is that the modes appear to evolve from being pinned at lower frequencies to being unpinned at higher frequencies. The frequencies of the one-dimensional even- and odd-node modes shown in Figs. 2 and 4 display an interesting interleaving property, at least at higher order: If ν_n is the frequency (in GHz) of the n-node mode, then $\nu_n < \nu_{n+1}$ for $n=4,5,\ldots,11$. Only the bulk mode does not fit this pattern. Also, note that with a frequency discrimination of 0.63 GHz we may observe two very different modes at the same frequency; for example, the bulk mode and the 5-node mode are both at 52 GHz.

In addition to the one-dimensional plane-wave-like solutions shown in Figs. 2 and 4, the simulations reveal the existence of several other types of modes. Figure 5 shows four modes that exhibit a two-dimensional structure. The top two modes are excited by the symmetric perturbation, the bottom two by the antisymmetric perturbation. These modes can be construed as standing waves with two orthogonal wave vectors. Note that, again, symmetric perturbations excite only symmetric modes, antisymmetric perturbations only antisymmetric modes. The two-dimensional normal modes display an interleaving property that is somewhat similar to the interleaving property observed for the one-dimensional modes: If ν_{n_x,n_z} is the frequency (in GHz) of the $n_x \times n_z$ mode, then $\nu_{n_x,n_z} < \nu_{n_x+1,n_z}$ for $n_x=3,4,\ldots,11$ and $n_z=2$. (The simulations did not reveal an obvious pattern for other values of n_z.)

While in the conventional ''standing-wave'' model (with pinned or unpinned boundary conditions) all modes of a rectangular sample are of the standing-wave type, we identified several modes that do not fit this description. For example, some modes are clearly localized in the particle near the edges or near the corners. Figure 6 shows two ''end modes'' that are localized near the edges, one generated by the symmetric perturbation (top), the other by the antisymmetric perturbation (bottom). These edge modes happen to have the same frequency (31 GHz) within the resolution of the simulations (0.63 GHz), which shows that selective excitation via the symmetry of the perturbation is essential. The fact that the frequency of the end modes is lower than the frequency of the bulk mode (52 GHz) can be traced to the larger local demagnetizing fields near the ends. In total, we have been able to identify more than 20 different normal modes. If we had applied antisymmetric perturbations along the z axis as well, we would presumably have detected at least another 20 modes. Although the modes can be sorted into families based on the number of nodal lines, even this classification is confusing because there exist modes with the same nodal structure but different frequencies that appear to differ only in the distribution of their amplitudes. At this stage of our understanding, there appears to be little reason to present the frequency and a full description of each one of them.

B. Variable applied field

Next, we investigate the variation of the mode frequencies with the strength of the applied field. Figure 7 shows the mode frequencies of the bulk mode (Fig. 2, second from top)—circles, the standing-wave mode with 10 nodes (Fig. 2, bottom)—triangles, and the symmetric end mode (Fig. 6, top)—diamonds. In general, the mode frequency increases with the number of nodes. The 11- and 12-node modes lie above the 10-node mode; the other standing-wave modes identified in the preceding section lie above or close to the bulk-mode frequency. The solid line in Fig. 7 is the Kittel FMR frequency of a three-dimensional ellipsoid with the same major axes as our particle.[30] In spite of its deviations from perfect uniformity, the frequency of the bulk mode is still in surprisingly good agreement with the Kittel equation for the uniform mode of a three-dimensional ellipsoid. The good agreement at high fields indicates that the average dipolar fields within the sample are similar to the homogeneous demagnetizing field within a comparable ellipsoidal sample. At low fields, the inhomogeneities of the demagnetizing fields become comparable to those of the applied field, and the agreement is less good. For which particle shape and/or size this agreement ceases to exist altogether remains to be determined.

Except for the end mode, the field dependence of the frequencies is very close to linear and shows no anomalous behavior at low fields. The end mode, however, shows considerable nonlinearity at low fields and extrapolates to zero frequency at approximately 1.1 kOe. Furthermore, although the symmetric and antisymmetric end modes are unresolved at high fields, the latter lies below the former at the lowest fields and extrapolates to zero frequency at approximately 1.2 kOe. The existence of zero-frequency modes is intimately related to the static instabilities of the magnetization. Although it is tempting to associate the zero frequency of the antisymmetric end mode with the onset of magnetization reversal, prior to any such interpretation one must investigate the possibility that other normal modes (for example, corner modes) could have zero frequency at higher fields.

C. Wavelength dependence of mode frequencies

It is instructive to compare the frequencies of the standing-wave modes with limiting cases of standing waves

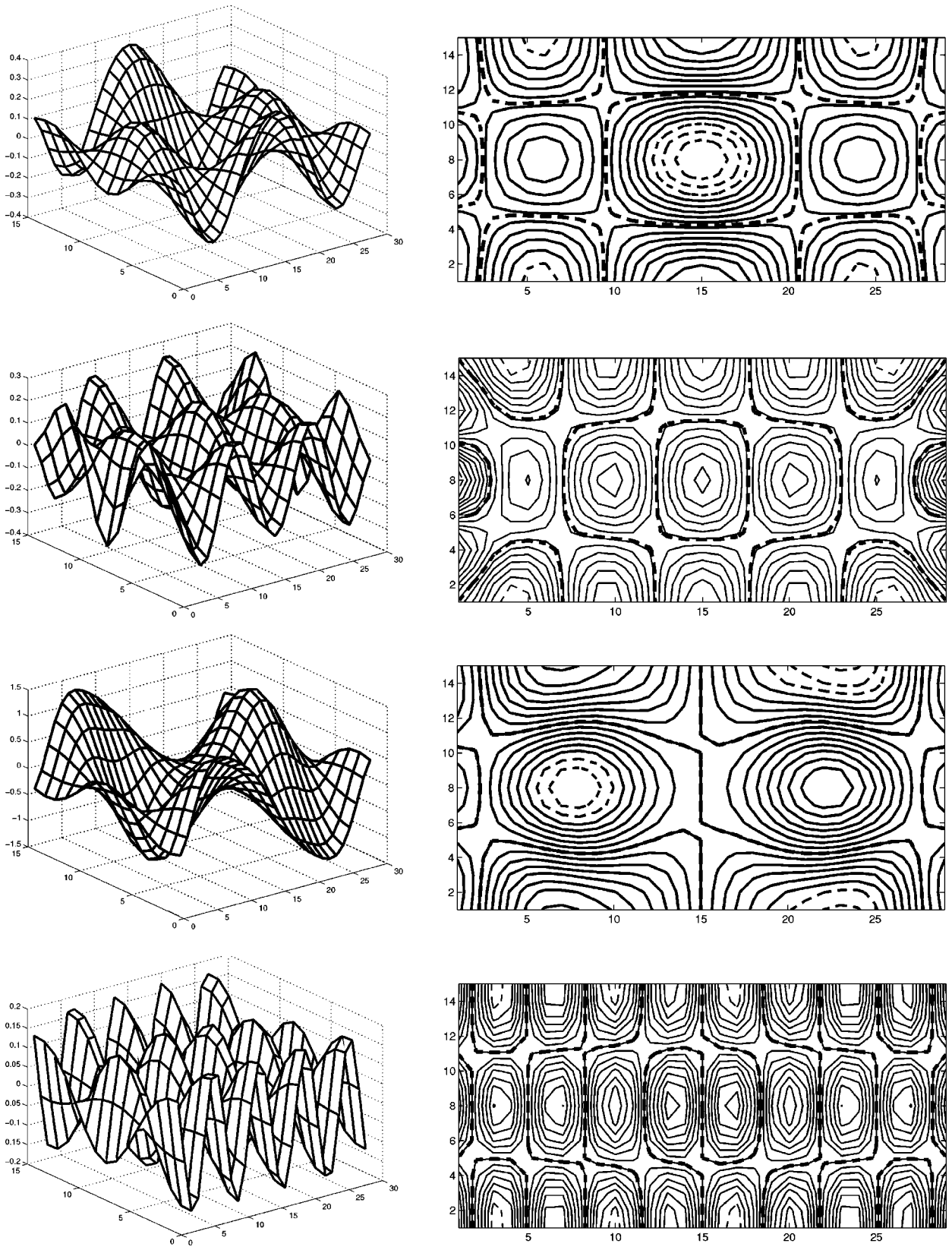

FIG. 5. Four two-dimensional modes. From top to bottom: 4×2 mode (64 GHz), 6×2 mode (73 GHz), 3×2 mode (64 GHz), and 9 ×2 mode (95 GHz).

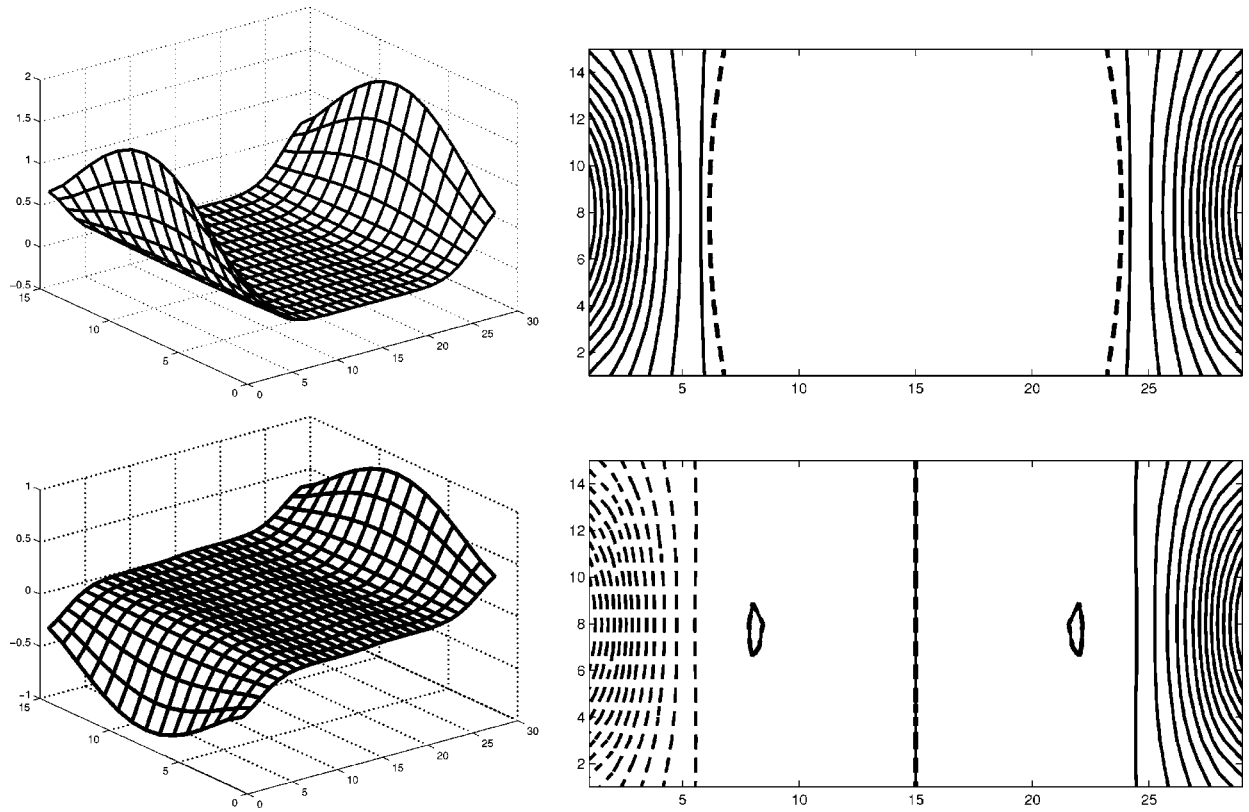

FIG. 6. Symmetric and antisymmetric end modes (31 GHz).

in a truncated infinite plate. In Fig. 8, we show the frequencies (at 10 kOe) of the standing-wave modes as a function of their wave vector. The wave vector of each mode was computed from the distance between nodal lines in Figs. 2 and 4; for the bulk mode, we assumed that the ''nodes'' were at the sample ends, so the wavelength was $2L$ and the wave vector $q=\pi/L$. If exchange is ignored, the frequency of modes propagating in an infinite plate along the magnetization direction is given by the formula[9,10]

$$\nu=\gamma\{H[H+\chi(q)4\pi M]\}^{1/2}, \tag{21}$$

where χ is a function of the wave vector q; $\chi(q)$ is found by solving a transcendental equation; its value decreases monotonically from 1 at $q=0$ to 0 at $q=\infty$. On the other hand, if dipolar fields are ignored and only the effects of exchange are included, the frequency is given by the formula

$$\nu=\gamma(H+Dq^2), \tag{22}$$

where D is the spin-wave stiffness constant. The predictions of Eqs. (21) and (22) are shown by the dashed-dotted and dashed lines in Fig. 8. It is possible[14] to incorporate the effects of exchange and dipolar coupling by combining (although such an action is not mathematically rigorous) the two equations (21) and (22),

$$\nu=\gamma\{(H+Dq^2)[H+Dq^2+\chi(q)4\pi M]\}^{1/2}. \tag{23}$$

The frequency ν given by Eq. (23), with the value $D=2.2\times10^{-9}$ Oe cm^2 for bulk Fe, gives the full line in Fig. 8. Considering that Eq. (23) describes a perfect standing spin wave, where the phase and the orbital aspect ratio are constant and the tilt is zero, we see that it provides a surprisingly good description of the wave-vector dependence of the mode frequencies, even in the crossover region where both dipolar and exchange contributions are comparable.

The wave vectors of the normal modes also warrant attention. In a standing-wave model, the allowed wave vectors are given by $q=q_n=n\pi/L$, where L is the length of the sample; if full pinning is assumed (zero amplitude at the ends), $n=1,2,\ldots$; if the ends are unpinned (maximum amplitude at the ends), $n=0,1,2,\ldots$. Although the pinning boundary conditions have been debated for many years, recent studies[15,16] have shown that an effective pinning is induced by the dipolar forces near the edges. The same authors also report that, while the longer wavelength modes are pinned at the ends, the short wavelength modes are essentially unpinned. Our simulations show that, for the model particle considered in the present investigation, the crossover from pinned to unpinned occurs roughly between the modes with 4 and 5 nodes.

D. Additional observations

While developing the techniques and obtaining the results presented above, we encountered numerous aspects that deserve further and more detailed investigation.

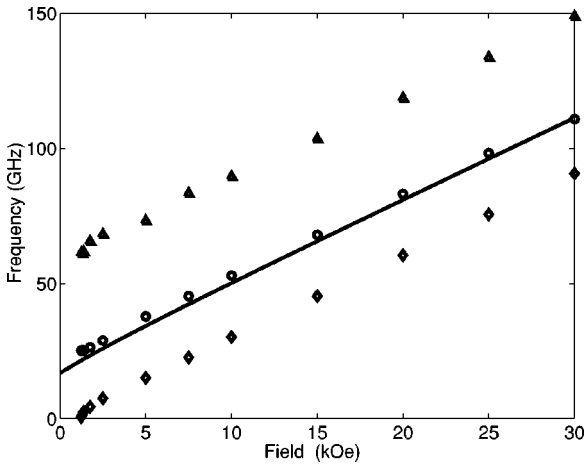

FIG. 7. Variation of mode frequencies with the applied field: bulk mode (circles), 10-node mode (triangles), end mode (diamonds). The solid line is the Kittel FMR frequency of an ellipsoid with the same major axes as our particle.

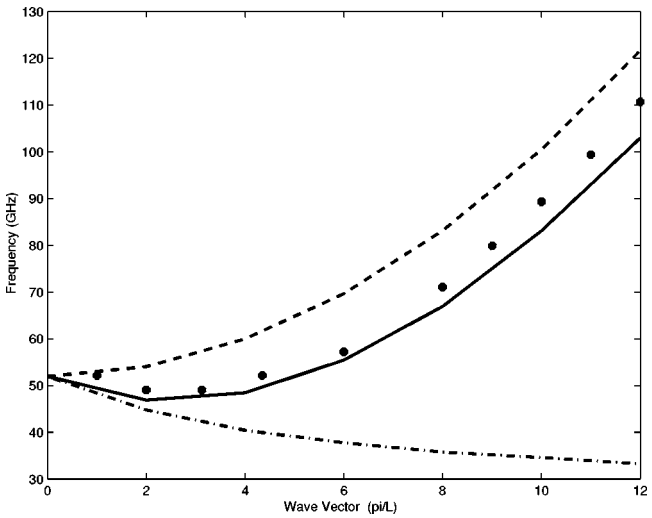

FIG. 8. Variation of the normal-mode frequencies (at $H_a = 10$ kOe) with their wave vector. The dots represent the computed results; the dot-dashed, dashed, and full line correspond to Eqs. (21), (22), and (23), respectively.

(i) We observed that two modes, namely, the bulk mode and the 5-node mode, crossed as the field was increased. In this particular case, the symmetric and antisymmetric nature of the two modes precludes hybridization effects. However, one can envision cases where a crossover occurs while hybridization is allowed, and such cases could be investigated with the present formalism.

(ii) Large-amplitude perturbations lead to changes in the peak positions in the Fourier transform. This result indicates that the nonlinear response regime can also be probed with the technique described here.

(iii)At low fields, where the static magnetization profile no longer has the symmetry of the particle (that is, a C-like state), many more low-frequency modes of the end-mode type were excited.

(iv) We also found that, while at high fields most of the amplitude is concentrated in the bulk mode, the energy of the end modes grows by several orders of magnitude relative to the bulk mode as the applied field decreases.

IV. SUMMARY AND CONCLUSIONS

In this paper we have developed a computational approach, based on the Landau-Lifshitz formalism of micromagnetics, to identify the magnetic normal modes of a nanosized particle. The formalism is general and applies to particles of any shape and material in an applied field of arbitrary direction and strength.

We have applied the technique to a rectangular model of a polycrystalline iron particle measuring $116\times20\times60$ nm^3. We find modes that, although reminiscent of standing spin waves, are considerably more complex. The elliptical spin orbits may be tilted with respect to the sample axes, and the modes have a spatially varying phase. Our simulations also show the existence of modes that are clearly localized, for example, near the edges or corners of the particle. These modes have frequencies well below those of the spin-wave modes. Moreover, their frequency extrapolates to zero at field values close to the value at which the static magnetization loses the symmetry of the particle—a strong indication that these modes are closely tied to the onset of the magnetization reversal process.

The technique and results presented here show that it is possible to obtain both the frequencies and the profiles of the normal modes of a magnetic particle, irrespective of its size and shape and independently of the spatial extent of the modes. The micromagnetic approach thus enables us to bridge the gap between spin-wave theory, where demagnetizing fields are largely ignored, and magnetostatic theory, where exchange is ignored. In fact, with the magnetostatic approach it has been possible to obtain only approximate solutions for particles with a relatively simple shape.[11,12] The present formalism does not suffer from this limitation.

The results of our investigation demonstrate the potential of the proposed computational approach. Future studies must be directed at extending the study beyond the simple case considered here. In principle, the technique can be used to determine not just the magnetic normal modes of a given particle but also their general dependence on the material parameters and on particle shape and size. Since the technique requires, however, considerable computational effort, it must be used selectively to address well defined problems in nanomagnetism. Examples are mode instabilities determining or contributing to magnetization reversal, normal modes of magnetic vortex states, normal modes of ring structures, and the wave-vector dependencies of edge modes and end modes. At present, no other suitable technique is available to address these problems in their most general form.

ACKNOWLEDGMENTS

The work of G.L., H.K., and D.K. was supported by the Mathematical, Information, and Computational Sciences Division subprogram of the Office of Advanced Scientific Computing Research, Office of Science, U.S. Department of Energy, under Contract No. W-31-109-Eng-38. M.G. was supported by the Basic Energy Sciences/Materials Sciences program of the U.S. Department of Energy, under Contract No. W-31-109-ENG-38. The work of R.C. was supported by U.S. Army Research Office Grant No. DAAD-19-02-1-0174.

*Electronic address: grimsditch@anl.gov;
URL: http://www.msd.anl.gov/groups/mf/index.html
†Electronic address: leaf@mcs.anl.gov;
URL: http://www. mcs.anl.gov/~leaf
‡Electronic address: kaper@mcs.anl.gov;
URL: http://www.mcs.anl.gov/~kaper
§Electronic address: karpeev@mcs.anl.gov;
URL: http://www.mcs.anl.gov/~karpeev
¶Electronic address: rcamley@uccs.edu;
URL: http://www.uccs.edu/~physics/faculty.html

[1] W. Wu, B. Cui, X.-Y. Sun, W. Zhang, L. Zhuang, L. Kong, and S.Y. Chou, J. Vac. Sci. Technol. B **16**, 3825 (1998).
[2] R.D. Gomez, T.V. Luu, A.O. Pak, I.D. Mayergoyz, K.J. Kirk, and J.N. Chapman, J. Appl. Phys. **85**, 4598 (1999).
[3] T.A. Savas, M. Farhoud, H.I. Smith, M. Hwang, and C.A. Ross, J. Appl. Phys. **85**, 6160 (1999).
[4] A. Fernandez and C.J. Cerjan, J. Appl. Phys. **87**, 1395 (2000).
[5] R.M.H. New, R.F.W. Pease, and R.L. White, J. Magn. Magn. Mater. **155**, 140 (1996).
[6] M. Farhoud, H.I. Smith, M. Hwang, and C.A. Ross, J. Appl. Phys. **87**, 5120 (2000).
[7] N. Smith and P. Arnett, Appl. Phys. Lett. **78**, 1448 (2001).
[8] C. Herring and C. Kittel, Phys. Rev. **81**, 869 (1951).
[9] J. Eshbach and R. Damon, Phys. Rev. **118**, 1208 (1960).
[10] R.W. Damon and J. Eshbach, J. Phys. Chem. Solids **19**, 308 (1961).
[11] L.R. Walker, J. Appl. Phys. **29**, 318 (1958).
[12] L.R. Walker, Phys. Rev. **105**, 390 (1957).
[13] V.A. Ignatchenko and R.S. Iskhakov, Zh. Eksp. Teor. Fiz. **72**, 1005 (1977) [Sov. Phys. JETP **45**, 526 (1977)].
[14] S.O. Demokritov, B. Hillebrands, and A. Slavin, Phys. Rep. **348**, 441 (2001).
[15] J. Jorzick, S.O. Demokritov, B. Hillebrands, M. Bailleul, C. Fermon, K.Y. Guslienko, A.N. Slavin, D.V. Berkov, and N.L. Gorn, Phys. Rev. Lett. **88**, 047204 (2002).
[16] K. Guslienko, S. Demokritov, B. Hillebrands, and A. Slavin, Phys. Rev. B **66**, 132402 (2002).
[17] K.Y. Guslienko, R.W. Chantrel, and A.N. Slavin, Phys. Rev. B **68**, 024422 (2003).
[18] L. Landau and E. Lifshitz, Phys. Z. Sowjetunion **8**, 153 (1935).
[19] V. Novosad, M. Grimsditch, K. Guislenko, P. Vavassori, Y. Otani, and S. Bader, Phys. Rev. B **66**, 052407 (2002).
[20] S. Jung, J. Ketterson, and V. Chandrasekhar, Phys. Rev. B **66**, 132405 (2002).
[21] J.P. Park, P. Eames, D.M. Engebretson, J. Berezovsky, and P.A. Cromwell, Phys. Rev. Lett. **89**, 277201 (2002).
[22] J.S. Jiang, H.G. Kaper, and G.K. Leaf, Discrete Contin. Dyn. Syst., Ser. B **1**, 219 (2001).
[23] W. Chen, D.R. Fredkin, and T.R. Koehler, IEEE Trans. Magn. **29**, 2124 (1993).
[24] D. Lewis and N. Nigam, *Proceedings of Third SIAM Conference on Mathematical Aspects of Materials Science, Philadelphia, Pennsylvania, 2000* (unpublished).
[25] W.E and X.P. Wang, http://www.math.princeton.edu/~weinan/papers/LL1.pdf
[26] D. Fredkin and T. Koehler, IEEE Trans. Magn. **26**, 415 (1990).
[27] C. Kittel, Phys. Rev. **110**, 1295 (1958).
[28] M. Seavey and P. Tannenwald, Phys. Rev. Lett. **1**, 108 (1958).
[29] G.T. Rado and J.R. Weertman, J. Phys. Chem. Solids **11**, 15 (1959).
[30] C. Kittel, Phys. Rev. **71**, 270 (1947).